CHEMMEDCHEM

DOI: 10.1002/cmdc.200900373

Discovery of Potent Vascular Endothelial Growth Factor Receptor-2 Inhibitors

Athanasios Papakyriakou,[a] Maria E. Katsarou,[a] Maria Belimezi,[b] Michael Karpusas,[c] and Dionisios Vourloumis*[a]

Substantial evidence over the last decades has implicated uncontrolled angiogenesis with various pathological states, including cancer. Vascular endothelial growth factor (VEGF) plays a critical role in its regulation. Because the tyrosine kinase VEGF receptor-2 (VEGFR-2) is the major mediator of the mitogenic, angiogenic, and permeability-enhancing effects of VEGF, it has become one of the most profound anti-angiogenesis targets. Inspired by the anthranilamide class of VEGFR-2 inhibitors, we performed a computational analysis of some potent representative members, using docking and molecular dynamics calculations. Based on the observations drawn from introducing the effect of the receptor's flexibility in implicit aqueous environment, we designed, synthesized, and characterized several new analogues of related scaffolds with modifications in their steric and electronic characteristics. In vitro evaluation of these compounds revealed several novel VEGFR-2 inhibitors that are less cytotoxic and more potent than the parent compounds.

Introduction

Vascular endothelial growth factor (VEGF) plays a critical role in the regulation of angiogenesis, the process that leads to the formation of new blood vessels.[1] Substantial evidence over the last decades implicates uncontrolled angiogenesis with various pathological states such as psoriasis, diabetic retinopathy, rheumatoid arthritis, chronic inflammation, and cancer.[2] VEGF exerts its cellular effects mainly by interacting with two high-affinity transmembrane tyrosine kinase receptors (RTKs): VEGFR-1 (Flt-1) and VEGFR-2 (KDR human/Flk-1 mouse).[3] Inhibition of VEGF or its receptor signaling system is therefore an attractive target for therapeutic intervention,[4,5] as exemplified by the recent USFDA approval of a humanized anti-VEGF monoclonal antibody (bevacizumab, Avastin®) as a first-line treatment for metastatic colorectal cancer, in combination with chemotherapy.[6]

Both VEGFR-1 and VEGFR-2 have seven Ig-like extracellular domains, a single-transmembrane region, and a consensus tyrosine kinase sequence that is interrupted by a kinase insert domain.[7] Their kinase domains are highly conserved, with about 70% sequence identity, whereas the C-terminal region is the most differentiated.[7] On the surface of vascular endothelial cells, VEGFR-2 undergoes dimerization upon strong binding of VEGF homodimers, albeit with lower affinity than VEGFR-1.[5] The activity of both receptors is mediated by ligand-dependent tyrosine autophosphorylation in the intracellular kinase domain which catalyzes the phosphorylation of cytosolic substrate proteins and downstream cellular events.[8,9] Among several tyrosine residues that have been shown to be phosphorylated, two major VEGF-dependent autophosphorylation sites have been identified in VEGFR-2; however, only the autophosphorylation of Tyr1175 has been identified as crucial for VEGF-dependent endothelial cell proliferation.[10]

Based on the universally accepted hypothesis that VEGFR-2 is the major mediator of the mitogenic, angiogenic, and permeability-enhancing effects of VEGF,[5] the specific receptor has become one of the most profound anti-angiogenesis targets.[11] Consequently, a significant number of small-molecule inhibitors has been developed during the last few years,[12–15] comprising derivatives of phthalazines, anthranilamides, disubstituted ureas, indolin-2-ones, quinazolines, quinolines, pyrimidines, pyridines, triazines, thiazoles, oxazoles, imidazoles, indazoles, indenopyrrolocarbazolones, and other miscellaneous compounds.[15] The availability of high-resolution X-ray crystal structures of the kinase domain of human VEGFR-2,[16] as well as co-crystallization data of the receptor with small-molecule binders,[17–24] has greatly enhanced important structure–activity relationship studies.

A representative example of VEGFR-2 inhibitors is the anthranilamides, designed based on the hypothesis that an intramolecular hydrogen bond between the aniline and the benzanilide carbonyl group would favor a conformation with a high degree of similarity to that of the previously discovered phthalazine class (Scheme 1).[25] Lead optimization studies within the

[a] Dr. A. Papakyriakou, Dr. M. E. Katsarou, Dr. D. Vourloumis
Laboratory of Chemical Biology of Natural Products and
Designed Molecules, Institute of Physical Chemistry, NCSR "Demokritos"
15310 Ag. Paraskevi Attikis, Athens (Greece)
Fax: (+30) 210-6511766
E-mail: vourloumis@chem.demokritos.gr

[b] Dr. M. Belimezi
Regulon A.E., Afxentiou 7, 17455 Alimos Attikis, Athens (Greece)

[c] Dr. M. Karpusas
Laboratory of Physics, Department of Science
Agricultural University of Athens, Iera Odos 75, 11855 Athens (Greece)

Supporting information for this article is available on the WWW under http://dx.doi.org/10.1002/cmdc.200900373.

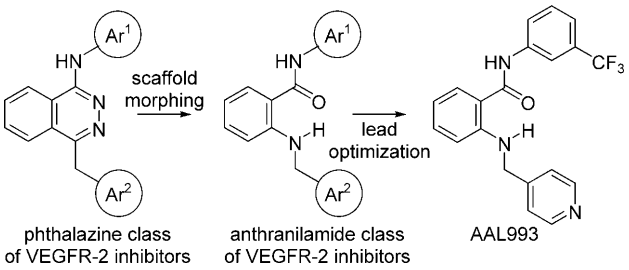

Scheme 1. Evolution of the phthalazine class of VEGFR-2 inhibitors to the anthranilamides, and the structure of AAL993 as a representative example of the latter.

anthranilamide series resulted in the identification of AAL993 (Scheme 1) as a highly potent and selective inhibitor of VEGFRs, with good pharmacological properties and excellent oral bioavailability, in both rodents and dogs.[26] The X-ray crystal structure of AAL993 in complex with the catalytic domain of diphosphorylated VEGFR-2 revealed that this molecule binds to and stabilizes the inactive conformation of the protein.[27] Despite the high structural conservation of RTKs bound to the ATP-active configuration, the inactive states of these enzymes often adopt distinct conformations, presenting large variations in the size and shape of the ATP-binding pocket.[28] As a consequence, it was suggested that targeting such inactive conformations would provide an attractive strategy for achieving target selectivity.[28]

In our studies we employed docking calculations in conjunction with molecular dynamics (MD), aiming to provide receptor–drug models that implicate both the flexibility of the kinase domain and the effect of the polar solvent in the observed binding affinity of the inhibitors.[29] Initially, molecular modeling of several designed anthranilamide scaffolds with alternative substitution patterns based on AAL993 was pursued. Based on our observations the central phenyl ring could be replaced by thiophene, which could potentially alter the electronic characteristics of the newly designed ligands, optimizing their binding affinity. These analogues were synthesized and screened in vitro for their inhibitory potential toward VEGFR-2. Furthermore, the analogous anthranilamides were generated for direct biological comparison. Our overall results were analyzed by computational methods.

Results

As reported for the AAL993–VEGFR-2 complex,[27] the inhibitor binds to the protein through three hydrogen bonds between: a) the pyridine N atom and the backbone NH of Cys 919 in the hinge region of the protein, b) the anthranilamide C=O group and the backbone NH of Asp 1046 of the conserved DFG motif, and c) the anthranilamide NH and the side chain carboxylate of Glu 885 of the αC helix. The trifluoromethylphenyl moiety of AAL993 is accommodated within a lipophilic pocket defined by residues Ile 888, Leu 889, Ile 892, Val 898, Val 899, Leu 1019, and Ile 1044, while the phenyl ring of the anthranilamide moiety is sandwiched between the hydrophobic side chain components of Val 914 and Lys 868. For the initial stages of our modeling effort, we prepared a model of the AAL993–VEGFR-2 complex based on the available X-ray structures of other complexes (see *Computational methods* in the Experimental Section and Figure 1 A). The docking results were analyzed based on the reported characteristics of the compound's interaction with the biological target. Thus, the choice of the docked conformation was based solely on structural and not energetic cri-

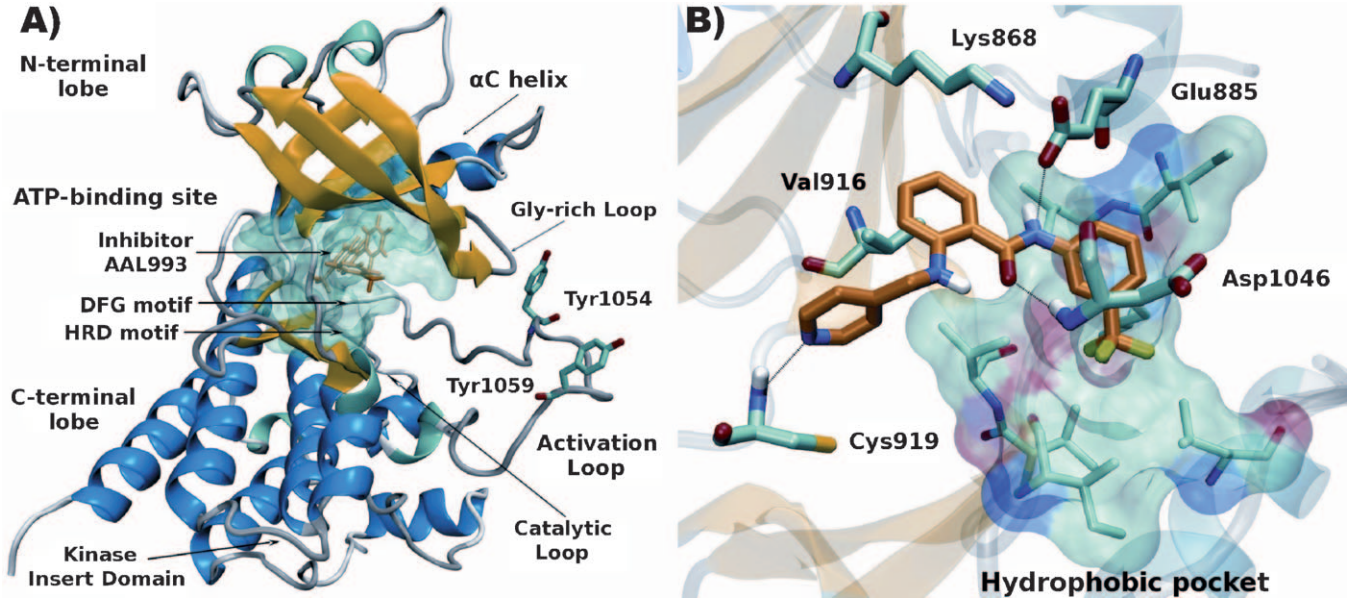

Figure 1. A) Model of VEGFR-2 kinase domain based on the X-ray crystal structure (PDB entry 1YWN).[18] The location of AAL993 in the ATP binding site is illustrated by the light green surface. Also indicated are the activation loop, the catalytic loop, the αC helix, the Gly-rich loop, and the two Tyr residues of the activation loop that were found to be autophosphorylated. B) Close-up view of AAL993 (stick representation; C atoms in orange) docked into the ATP binding site of VEGFR-2. Residues of the kinase domain (C atoms in light green) that mediate key H-bonding interactions are labeled. The trifluoromethylphenyl moiety of AAL993 is buried inside a hydrophobic pocket, which is depicted as a surface. Nitrogen atoms are shown in blue, oxygen in red, sulfur in yellow, and fluorine in green.

teria, that is, higher-binding-energy models were discarded when they did not exhibit the three key interactions mentioned above (Figure 1 B).

Our MD calculations employed the inactive "DFG-out" conformation of VEGFR-2 as previously reported.[27] A 10-ns MD simulation, carried out with AAL993 docked at the ATP binding site, predicted that some of the previously mentioned key interactions are not well conserved in the presence of solvent (figure S1, Supporting Information). In particular, the distance between the anthranilamide NH and the carboxylate of Glu 885 fluctuates largely as a function of the simulation time. Similarly, the pyridine N atom and the side chain amide of Cys 919 are within H-bonding distance for less than 50% of the simulation time. Because Cys 919 is one of the two residues, the other being Glu 917, in the hinge region that interacts with the adenine of ATP, it represents a primary target for ligand design. On the other hand, the trifluoromethylphenyl group of the inhibitor is well accommodated within the lipophilic pocket that consists of residues Ile 888, Leu 889, Ile 892, Val 898, Val 899, Leu 1019, and Ile 1044, thus maintaining their hydrophobic contacts throughout the major part of the MD simulation (figure S2, Supporting Information). Based on these observations we hypothesized that substituting either the pyridine group or the central phenyl group in the anthranilamide series might yield improved inhibitors of VEGFR-2.

Synthesis

The targeted anthranilamides were readily prepared in two steps,[26] as presented in Scheme 2. Thus, ring opening of isatoic anhydride **2** with 3-trifluoromethylaniline **1** afforded amide **3**, which upon reductive alkylation with aldehydes RCHO (**a**–**j**) produced the corresponding anthranilamides **4a**–**4j**. AAL993 was also synthesized by the same reaction sequence (**4a** in Scheme 2) for direct biological comparisons. The majority of

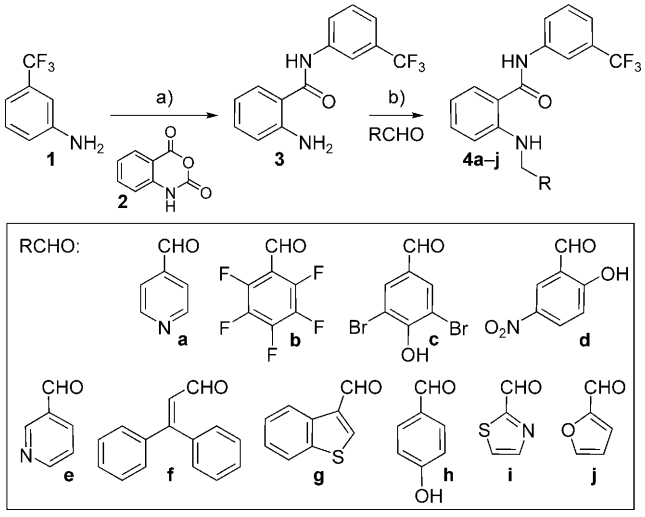

Scheme 2. Reagents and conditions: a) **1** (1.0 equiv), **2** (1.0 equiv), DMF (0.62 M), 100 °C, 24 h, 36%; b) AcOH (3.0 equiv), RCHO (1.3 equiv), MeOH (0.07 M), 23 °C, 8 h, then $NaCNBH_3$ (4.4 equiv), 23 °C, 24 h, 28–91%. DMF = *N*,*N*-dimethylformamide.

the selected aldehydes comprise heteroatoms capable of interacting with Cys 919 of the hinge region through hydrogen bonding. The differential topology of the heteroatoms would serve in the investigation of the target's flexibility as well as the solvation effects. Aldehydes **b** and **f** were specifically employed to explore the potential of extensive hydrophobic contacts compensating for the loss of the aforementioned key interaction.

The thiophene-containing analogues were synthesized according to the procedure presented in Scheme 3. Specifically, protection of methyl-3-aminothiophene-2-carboxylate **5** with

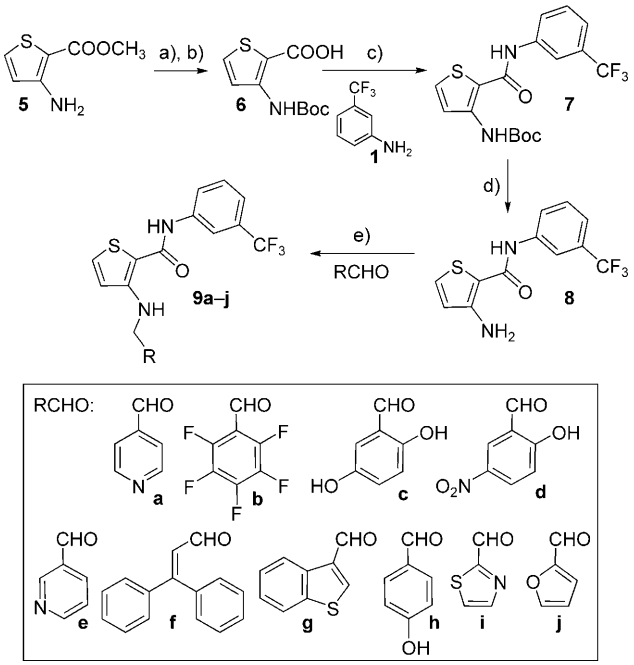

Scheme 3. Reagents and conditions: a) **5** (1.0 equiv), Boc_2O (3.1 equiv), Et_3N (20% in CH_2Cl_2), DMAP (1.6 equiv), 23 °C, 4 h, 80%; b) NaOH (0.6 M in H_2O/MeOH 1:20), 23 °C, 6 h, 98%; c) **6** (1.0 equiv), **1** (3.0 equiv), DIC (4.0 equiv), DIPEA (4.1 equiv), DMAP (3.0 equiv), THF (0.60 M), 70 °C, 2 h, 52%; d) TFA (26% in CH_2Cl_2), 23 °C, 30 min, 99%; e) AcOH (4.1 equiv), RCHO (1.4 equiv), MeOH (0.07 M), 23 °C, 12 h, then $NaCNBH_3$ (4.7 equiv), 23 °C, 24 h, 57–95%. Boc = *t*-butyloxycarbonyl; DIC = *N*,*N*′-diisopropylcarbodiimide; DIPEA = *N*,*N*-diisopropylethylamine; DMAP = *N*,*N*-dimethylpyridin-4-amine; THF = tetrahydrofuran; TFA = trifluoroacetic acid.

Boc_2O afforded the corresponding N-protected ester, which was then hydrolyzed with sodium hydroxide in methanol to yield the N-protected aminothiophene-2-carboxylic acid **6**. Coupling of **6** with 3-trifluoromethylaniline **1**, mediated by DIC, followed by the removal of the protecting carbamate with TFA, furnished aromatic amine **8** in 52% yield for the two steps. Finally, **8** was employed in the reductive alkylation reactions with aldehydes RCHO (**a**–**j**, Scheme 3) to form compounds **9a**–**9j** in 57–95% yield.

Biological evaluation

The ability of the synthetic compounds to inhibit the proliferation of cell growth was determined by MTT assay, as described

previously.[30] MTT is absorbed by the mitochondria, where it is transformed into formazan by succinic dehydrogenase. By assessing mitochondrial dehydrogenase activity, the amount of viable cells in a cell population after treatment with each compound for various time periods can be measured. Therefore, the sensitivity of the cells to the concentration and incubation time with the various compounds can be determined. The absorbance of each cell lysate solution was measured at $\lambda =$ 550 nm. The results from the MTT assays are expressed as the means of the absorption values $A_{550} \pm$ SD using data from two independent experiments, which had each been repeated three times. CC_{50} values, representing the concentration of each compound required for a 50% decrease in cell viability, were estimated by sigmoid fit, and are listed in Table 1.

IC_{50} values for the inhibition of VEGFR-2 (KDR) kinase by individual compounds were measured with the HTScan® VEGFR-2 kinase assay kit (Cell Signaling Technology, USA), following the colorimetric ELISA protocol that was provided by the manufacturer. Recombinant human GST–VEGFR-2 kinase (Val 789–Val 1356), biotinylated peptide substrate and phosphotyrosine antibody, for the detection of phosphorylated substrate, were all supplied within the kit. Percent inhibition values were calculated using Equation (1), as detailed in the Experimental Section below. Each IC_{50} value was determined by plotting the percent inhibition as a function of log([compound] in nM) using a sigmoid fit and are presented in Table 1.

The four most potent compounds, **4a** (AAL993), **4e**, **9d**, and **9j**, were evaluated for their effect on angiogenesis by using an endothelial tube formation assay on an ECMatrix™ (Chemicon®). This solid gel consists of basement proteins (e.g., laminin, collagen type IV), growth factors (e.g., TGF-β), and proteolytic enzymes such as plasminogen and matrix metalloproteases that promote tube formation, a procedure requiring cell adhesion, migration, differentiation, and growth. Organization patterns in cells were observed after 4 h of culture. Qualitative assessment of images acquired at 6 h showed that **9d** and **9j** significantly inhibit the formation of capillary tubes, relative to compound **4a** and the control (Figure 2A,C). Quantitative analysis was also possible with an end-point assay, in which the capillary tube branch points were counted at 6 h. In the absence of VEGF, **4a** inhibited angiogenesis up to 60%, and **9j** up to 25% at both 10 and 50 $\mu g\,mL^{-1}$, while **9d** inhibited angiogenesis up to 35 and 58% at 10 and 50 $\mu g\,mL^{-1}$, respectively, relative to control (Figure 2B). Incubation of cells in combination with 50 $ng\,mL^{-1}$ VEGF (Figure 2D) almost entirely inhibited tube formation up to 90% for compound **9d** at both concentrations. Significant inhibition was observed for **4a** up to 65 and 80%, and for **9j** up to 80 and 65% at 10 and 50 $\mu g\,mL^{-1}$, respectively, relative to control. Compound **4e** exhibited the lowest inhibitory effect among the four inhibitors tested (data not shown).

Table 1. Potency data for the synthetic analogues **4a**–**4j** and **9a**–**9j**.

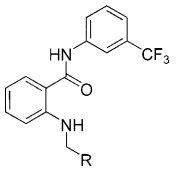

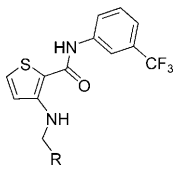

Compd	R	CC_{50} [μM]	IC_{50} [nM]	Compd	R	CC_{50} [μM]	IC_{50} [nM]
4a		146	40	**9a**		99	> 500
4b	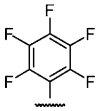	141	490	**9b**	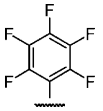	264	> 500
4c	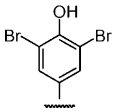	38	> 500	**9c**	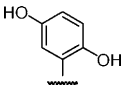	43	> 500
4d	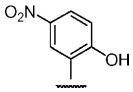	36	> 500	**9d**	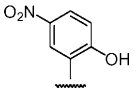	109	< 1
4e		105	3	**9e**		152	> 500
4f	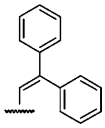	340	> 500	**9f**	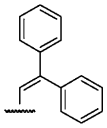	> 300	> 500
4g		349	> 500	**9g**		285	> 500
4h	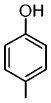	34	> 500	**9h**	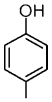	93	> 500
4i		229	> 500	**9i**		138	> 500
4j		153	> 500	**9j**		104	70

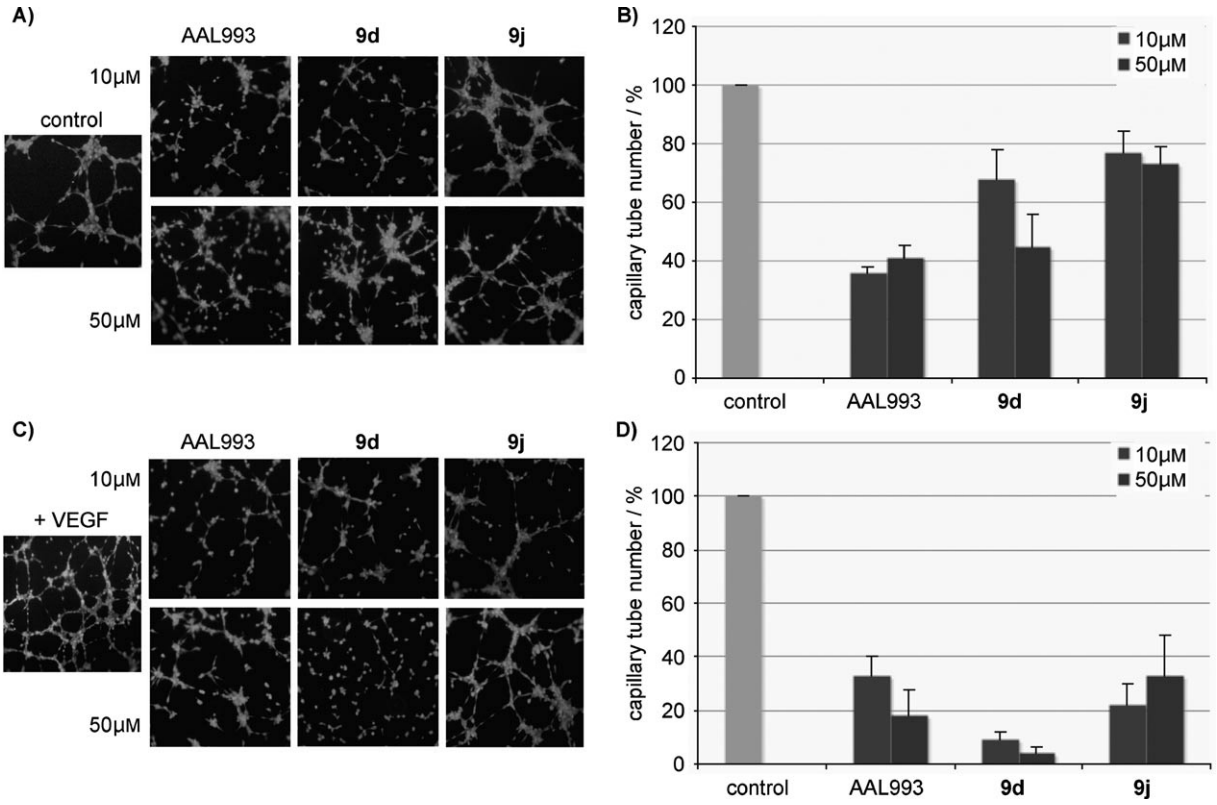

Figure 2. Tube formation assay after culture on ECMatrix™ for 6 h. HUVECs were stained with calcein and visualized by fluorescence microscopy. A) Control cells and cells treated with AAL993 (**4a**), **9d**, or **9j** at 10 or 50 μg mL^{-1}, as indicated. B) Number of capillary tube branch points of treated HUVECs compared with untreated cells (relative to control, set at 100%). C) Control cells and cells treated with AAL993 (**4a**), **9d**, or **9j** at 10 or 50 μg mL^{-1}, as indicated, in the presence of VEGF (50 ng mL^{-1}). D) Number of capillary tube branch points of treated HUVECs compared with untreated cells (relative to control, set at 100%) in the presence of VEGF (50 ng mL^{-1}). Data in graphs are expressed as the mean ± SD of three independent experiments; $p < 0.01$ relative to control.

Discussion

Our efforts to evaluate our results and extract useful conclusions regarding important conformational and structural data in the biological affinities of the synthetic analogues toward the protein target were assisted by computational methods. Although the absence of an exact crystal structure renders this method highly speculative, important interactions may be identified in the process, inspiring further development and directing future synthetic endeavors.

Specifically, substitution of the 4-pyridine functionality in AAL993 (**4a**) by 3-pyridine in compound **4e** resulted in a higher-affinity VEGFR-2 inhibitor (Table 1). This effect cannot be explained by examining the initial docked conformation of **4e**, owing to the clear resemblance with AAL993, which lacks the intermolecular hydrogen bond between the pyridine N atom and the NH group of Cys919. However, during the 10-ns MD calculations, it was recognized that the missing interaction was compensated by solvent molecules (W1–W3 in Figure 3), which mediate H-bonding contacts between the pyridine N atom and both the NH and C=O groups of Cys919. This effect is observed in approximately 80% of the total simulation time. Interestingly, the direct hydrogen bonding of the anthranilamide NH with the carboxylate of Glu885 is also substituted by a solvent-mediated interaction via a long-lived water molecule (3–4 ns, figure S3, Supporting Information), that is, W4 in Figure 3. Moreover, the side chain carboxylate groups of Glu885 and Asp1046 were found to be hydrogen bonded via solvent interactions (W5 and W6), while the backbone NH group of Asp1046 interacts directly with the anthranilamide C=O group.

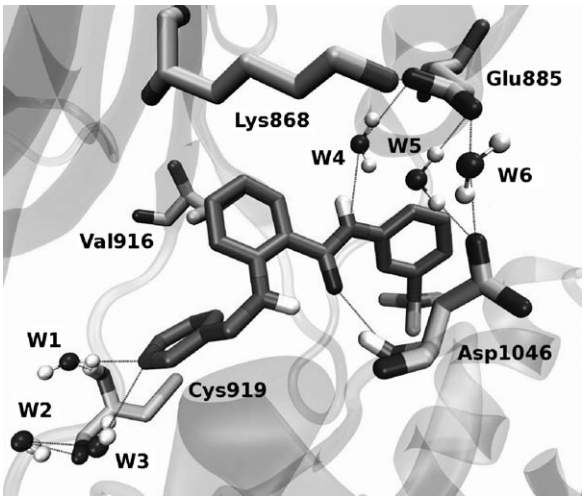

Figure 3. Snapshot at the end of a 10-ns MD simulation illustrating compound **4e** within the ATP binding cleft of VEGFR-2. Key residues of the kinase domain and water molecules (W1–W6) that mediate putative H-bonding interactions are depicted. The hydrophobic residues that interact with the trifluoromethylphenyl ring of **4e** are omitted for clarity.

Notably, the trifluoromethylphenyl ring retains the same hydrophobic interactions throughout the MD simulation, similar to AAL993 (Figure 1B). The above observations point to a binding model for compound **4e**, which mimics the same interactions as those reported for **4a** (AAL993), some of which, however, could be mediated by solvent molecules.

Docking of compound **9d** revealed a binding motif in which the trifluoromethylphenyl group is accommodated by the hydrophobic pocket while the amide NH is hydrogen bonded to Glu885, and the amide C=O group to the backbone NH of Asp1046 (Figure 4A). Additional stabilization of Asp1046 may be provided by the hydroxy group of **9d** through a hydrogen bond with its backbone carbonyl. At the same conformation, the nitro group forms ionic interactions with Arg1032, which is part of the catalytic loop, and is highly conserved among protein tyrosine kinases. In previous reports, Arg1032 was found to be hydrogen bonded to the side chain carboxylate of Asp1028 (HRD motif), which is essential for catalysis of the phosphotransfer reaction.[31] Alternatively, the nitro group may be oriented toward the hinge region, as observed throughout our MD simulations (Figure 4B). There it probably participates in two H-bonding interactions with the amide group of Cys919 and with the backbone of Glu917. In this conformation, the amide C=O of **9d** may accept two hydrogen bonds from Asp1046 NH and Cys1045 SH, while the amide NH may interact via water-mediated contacts with the carboxylate of Glu885. Further stabilization of Glu885 and Asp1046 side chains may involve solvent molecules, such as W5 shown in Figure 4B. A putative network of solvent molecules (W1–W4 in Figure 4B) is also predicted to mediate H-bonding interactions between the hydroxy group of **9d** and the backbone of Phe1047, Gly1048 (DFG motif), and Arg1032. It is therefore notable that in any of the predicted conformations, compound **9d** interacts with important residues of the ATP binding site, an effect that justifies its sub-nanomolar IC_{50} value for VEGFR-2 (Table 1).

Compound **9j** is predicted to bind within the ATP binding site in the same orientation as previously described (Figure 5). The trifluoromethylphenyl group is buried in the hydrophobic pocket, the amide NH is hydrogen bonded to the carboxylate of Glu885, and the amide C=O accepts a hydrogen bond from the Asp1046 backbone. Additionally, the amino group of **9j** may contribute to an increased stabilization of Asp1046 through hydrogen bonding. Interestingly, the thiophene ring is positioned ideally to interact with the terminal amine of Lys868, which provides electrostatic stabilization to Glu885. In this configuration, the furan oxygen atom of **9j** may readily accept a hydrogen bond from the side chain carboxamide of Asn1033. An additional interaction with Cys1045 (Figure 5) might be possible, as the furan oxygen is in the proximity of its sulfhydryl group (4.0 Å).

Concerning the synthetic analogues that lack hydrogen bonding potential (Schemes 2 and 3), as indicated by the perfluorobenzyl groups (in **4b** and **9b**) or the bulkier biphenyls

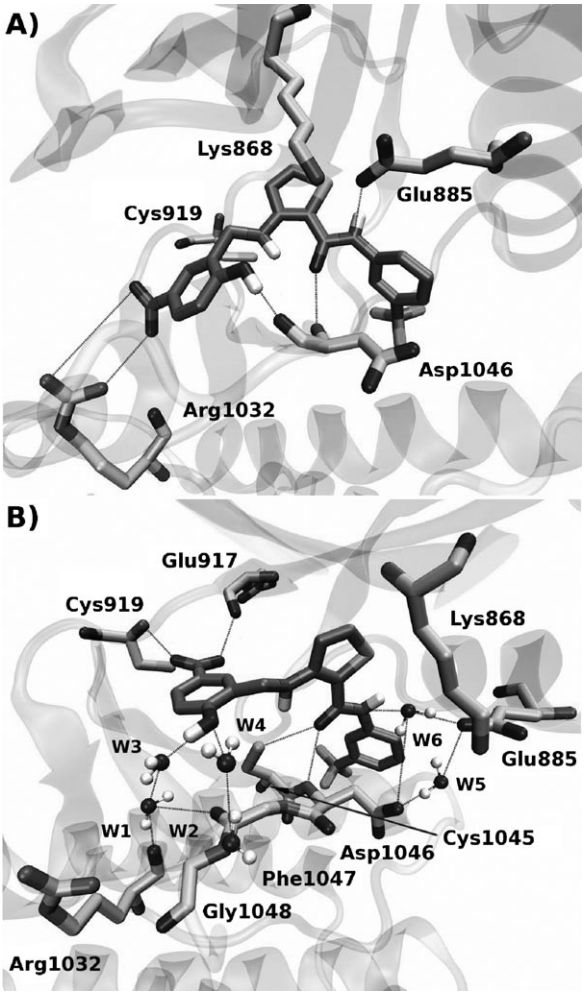

Figure 4. The different binding orientations of compound **9d** sampled during the MD simulations: docked configuration at A) 0 ns, and B) 10 ns. Residues of the VEGFR-2 kinase domain that provide key interactions and water molecules that mediate putative H-bonding interactions are depicted. The side chain atoms of Phe1047 and the residues that provide hydrophobic contacts are omitted for clarity.

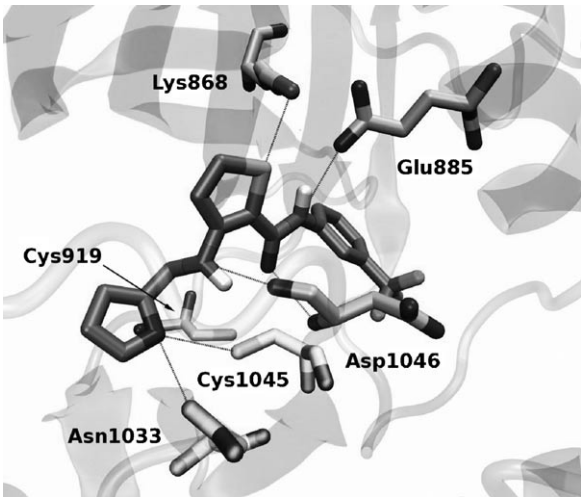

Figure 5. Intermolecular interactions of the simulated **9j**–VEGFR-2 complex. Key residues of the kinase domain are labeled, and residues that interact by hydrophobic contacts are omitted for clarity.

(in **4f** and **9f**), it is clear that the hydrophobic interactions initially targeted cannot compensate for the interaction with Cys919 of the hinge region. Similarly, the sulfur-bearing aromatic thiazoles **4i** and **9i**, as well as the benzothiophenes **4g** and **9g**, probably adopt unfavorable orientations to accept hydrogen bonds due to electronic or steric reasons, respectively. Compounds with phenolic hydroxy groups at the *para* position (**4c**, **4h**, and **9h**) were also found to be inactive (Table 1), indicating that steric hindrance does not allow the formation of the aforementioned hydrogen bond; on the other hand, such hydroxy groups contribute to the observed enhanced cytotoxicity (Table 1).

Great variation in the inhibitory potential between the two series is observed with R = 3- or 4-pyridine (Table 1). Specifically, the anthranilamide compounds **4a** and **4e** are highly active nanomolar inhibitors, while the respective thiophene-containing analogues **9a** and **9e** were found to be ineffective VEGFR-2 binders. Similarly, the inactive anthranilamides with R = 2-hydroxy-5-nitrobenzyl or 2-furan are transformed into the nanomolar thiophene-containing inhibitors **9d** and **9j**, respectively (Table 1). Clearly, there is a significant difference in the bound configurations between the two subfamilies. These results direct us to propose that substitution of the central benzene group by thiophene causes a change in the electronic properties of the designed scaffolds (figures S4 and S5, Supporting Information). It is therefore plausible that a change in the geometry of the intramolecular hydrogen bond at the constrained anthranilamides might result in altered conformational freedom of the thiophene-containing scaffolds, which might be responsible for additional interactions with key residues at the catalytic cleft. Furthermore, the thiophene sulfur atom might be directly implicated in H-bonding interactions with critical residues, as in the case of **9j**, which is predicted to provide additional stabilization for the Lys868···Glu885 pair (Figure 5).

Conclusions

Three novel low-nanomolar-range VEGFR-2 inhibitors have been discovered through a structure-based approach assisted by computational methods. MD analysis of the VEGFR-2–AAL993 complex has inspired the design and synthesis of a thiophene series of VEGFR-2 inhibitors with altered steric, electronic, and H-bonding requirements relative to the parent anthranilamides. The latter became clear by direct comparison of the biological activities between closely related analogues. In vitro evaluation of the two series both by KDR-specific kinase assays and HUVEC tube formation assays revealed their high anti-angiogenic potency. Moreover, a combination of docking and MD was used in order to formulate a reasonable explanation for the obtained results. Additional examples to assist us in the evaluation of this hypothesis and the establishment of a valid structure–activity relationship analysis, along with related selectivity studies and in vivo experiments, are currently under investigation.

Experimental Section

Chemistry

Unless otherwise noted, all solvents and reagents for organic synthesis were obtained from commercial suppliers and were used without further purification. All reactions were carried out under a dry Ar atmosphere with anhydrous, freshly distilled solvents under anhydrous conditions unless otherwise noted. All reactions were stirred with Teflon-coated magnetic stir bars, and temperatures were measured externally. Reactions requiring anhydrous conditions were carried out in oven-dried (120 °C, 24 h) or flame-dried (vacuum < 0.5 Torr) glassware. Yields refer to chromatographically and spectroscopically (^{1}H NMR) homogeneous materials. Reactions were monitored by thin-layer chromatography (TLC) carried out on 0.25 mm silica gel plates (60 F_{254}, E. Merck). Silica gel (60, particle size: 0.040–0.063 mm, E. Merck) was used for flash column chromatography.

NMR spectra were recorded on a Bruker Avance III-250 or a Bruker Avance DRX-500 instrument, as noted individually. All spectra were recorded at 298 K using deuterated solvents as internal standards: [$CDCl_3$, 7.26 ppm (^{1}H) and 77.16 ppm (^{13}C); [D_6]DMSO, 2.50 ppm (^{1}H) and 29.8 ppm (^{13}C)]. Chemical shift values (δ) are given within an accuracy of 0.01 ppm for ^{1}H NMR and 0.1 ppm for ^{13}C NMR data, while the coupling constants (J) are within 0.1 Hz. Multiplicities are designated as singlet (s), doublet (d), triplet (t), or multiplet (m). Broad or obscured peaks are indicated as "b" or "obs", respectively. 2D NMR ^{1}H–^{1}H COSY and ^{1}H–^{13}C HMQC correlation spectra were also recorded at 298 K in order to assist in peak assignment. The ^{1}H and ^{13}C NMR spectra of the most potent compounds **4a**, **4e**, **9d**, and **9j** are given in the Supporting Information.

2-Amino-*N*-[3-(trifluoromethyl)phenyl]benzamide (3).[26] A mixture of 3-trifluoromethylaniline **1** (500 mg, 3.1 mmol) and isatoic anhydride **2** (500 mg, 1.0 equiv, 3.1 mmol) in DMF (5 mL) was stirred at 100 °C for 24 h. The solvent was evaporated under reduced pressure to produce a residue which was dissolved in EtOAc (25 mL) and washed with saturated aqueous NH_4Cl (2×15 mL) and saturated NaCl (2×15 mL). The solution was dried using anhydrous $MgSO_4$, filtered, and the solvent was evaporated to provide the crude product, which was eluted from 10% EtOAc in hexanes to yield **3** as colorless needles (315 mg, 36%); ^{1}H NMR ([D_6]DMSO, 500 MHz): δ = 6.37 (bs, 2H), 6.60 (dd, J = 7.6, 7.4 Hz, 1H), 6.76 (d, J = 8.4 Hz, 1H), 7.22 (dd, J = 8.0, 7.6 Hz, 1H), 7.42 (d, J = 7.7 Hz, 1H), 7.57 (dd, J = 8.0, 7.7 Hz, 1H), 7.65 (d, J = 8.0 Hz, 1H), 7.97 (d, J = 8.1 Hz, 1H), 8.20 (s, 1H), 10.27 (s, 1H).

Compounds (4a–4j). A solution of **3** (210 mg, 0.75 mmol) and AcOH (50 μL, 2.9 mmol) in MeOH (10 mL) was divided among 10 flasks. Each solution was treated with 0.10 mmol of the corresponding aldehyde and stirred at ambient temperature for 8 h. The resulting reaction mixtures were treated with 1.0 mL of a solution of $NaCNBH_3$ (210 mg, 3.3 mmol) in MeOH (10 mL) and stirred for a further 24 h at ambient temperature. The solvent was evaporated, and the residues were diluted with CH_2Cl_2 (15 mL) and washed with saturated aqueous $NaHCO_3$ (2×10 mL) followed by saturated NaCl (2×10 mL). The organic layer was dried over $MgSO_4$, filtered, and concentrated under reduced pressure. All compounds were purified by column chromatography, eluted from EtOAc/hexanes:

2-[(4-Pyridyl)methyl]amino-*N*-[3-(trifluoromethyl)phenyl]benzamide (4a, AAL993). Colorless solid; R_f = 0.20 (EtOAc/hexanes, 1:1); (17 mg, 61%): ^{1}H NMR ([D_6]DMSO, 500 MHz): δ = 4.50 (d, J = 6.1 Hz, 2H), 6.55 (d, J = 8.5 Hz, 1H), 6.67 (dd, J = 7.4, 7.4 Hz, 1H), 7.26 (dd,

J=7.8, 7.4 Hz, 1H), 7.34 (bd, J=5.6 Hz, 2H), 7.45 (d, J=7.7 Hz, 1H), 7.59 (t, J=8.0 Hz, 1H), 7.73 (dd, J=7.9, 1.1 Hz, 1H), 7.94 (t, J=6.2 Hz, 1H), 7.97 (bd, J=8.2 Hz, 1H), 8.26 (bs, 1H), 8.49 (bd, J=5.8 Hz, 2H), 10.44 (s, 1H); ^{13}C NMR ($CDCl_3$, 62.5 MHz): δ=46.1, 112.5, 115.1, 116.0, 117.5 (q), 121.2 (q), 122.1, 123.7, 127.7, 129.7, 133.8, 138.6, 148.6, 149.7, 150.1, 168.4; HRMS (ESI) *m/z* calcd for $C_{20}H_{16}F_3N_3ONa$ [*M*+Na]$^+$: 394.1138, found: 394.1137.

2-(Perfluorobenzyl)amino-*N*-[3-(trifluoromethyl)phenyl]benzamide (4b). Colorless solid; R_f=0.75 (EtOAc/hexanes, 1:4); (24 mg, 70%): ^{1}H NMR ($CDCl_3$, 500 MHz): δ=4.52 (bs, 2H), 6.73 (dd, J=7.7, 7.4 Hz, 1H), 6.87 (d, J=8.4 Hz, 1H), 7.40 (m, 2H), 7.48 (dd, J=8.0, 7.9 Hz, 1H), 7.51 (d, J=7.9 Hz, 1H), 7.74 (d, J=8.0 Hz, 1H), 7.84 (s, 1H), 7.87 (bs, 1H); ^{13}C NMR ($CDCl_3$, 62.5 MHz): δ=35.0, 111.8, 115.6, 116.4, 117.4 (q), 121.3 (q), 123.8, 127.7, 129.7, 129.7, 134.0, 138.4, 148.9, 168.0; HRMS (ESI) *m/z* calcd for $C_{21}H_{12}F_8N_2ONa$ [*M*+Na]$^+$: 483.0714, found: 483.0713.

2-(3,5-Dibromo-4-hydroxybenzyl)amino-*N*-[3-(trifluoromethyl)-phenyl]benzamide (4c). Yellow solid; R_f=0.45 (EtOAc/hexanes, 1:1); (23 mg, 56%): ^{1}H NMR ($CDCl_3$, 500 MHz): δ=4.32 (bs, 2H), 5.85 (bs, 1H), 6.59 (d, J=8.4 Hz, 1H), 6.70 (dd, J=7.9, 7.5 Hz, 1H), 7.31 (dd, J=8.4, 7.8, 1H), 7.41 (d, J=7.7 Hz, 1H), 7.44 (bs, 2H), 7.49 (dd, J=8.0, 7.6 Hz, 1H), 7.53 (d, J=7.6 Hz, 1H), 7.74 (d, J=7.4 Hz, 1H), 7.90 (s, 2H), 7.99 (bs, 1H); ^{13}C NMR ($CDCl_3$, 62.5 MHz): δ=45.8, 110.3, 112.7, 115.0, 116.0, 117.4 (q), 121.2 (q), 123.7, 127.5, 129.7, 130.6, 133.3, 133.9, 138.5, 148.6, 149.7, 168.2; HRMS (ESI) *m/z* calcd for $C_{21}H_{15}Br_2F_3N_2O_2Na$ [*M*+Na]$^+$: 564.9345, found: 564.9347.

2-(2-Hydroxy-5-nitrobenzylamino)-*N*-[3-(trifluoromethyl)phenyl]-benzamide (4d). Bright yellow solid; R_f=0.40 (EtOAc/hexanes, 1:1); (32 mg, 91%): ^{1}H NMR ($CDCl_3$, 500 MHz): δ=4.51 (bs, 2H), 6.85 (m, 3H), 7.36 (dd, J=7.8, 7.8 Hz, 1H), 7.41 (d, J=7.8 Hz, 1H), 7.48 (dd, J=8.0, 7.8 Hz, 1H), 7.58 (d, J=7.8 Hz, 1H), 7.72 (d, J=8.0 Hz, 1H), 7.90 (s, 1H), 8.03 (dd, J=8.9, 2.5 Hz, 1H), 8.08 (s, 1H), 8.13 (d, J=2.5 Hz, 1H); ^{13}C NMR ($CDCl_3$, 62.5 MHz): δ=46.0, 114.5, 116.7, 117.1, 117.7 (q), 118.0, 118.7, 121.6 (q), 123.9, 124.3, 124.8, 125.2, 125.8, 127.6, 129.8, 133.9, 138.1, 141.1, 149.1, 162.0, 168.1; HRMS (ESI) *m/z* calcd for $C_{21}H_{16}F_3N_3O_4Na$ [*M*+Na]$^+$: 454.0985, found: 454.0987.

2-[(3-Pyridyl)methyl]amino-*N*-[3-(trifluoromethyl)phenyl]benzamide (4e). Colorless solid; R_f=0.25 (EtOAc/hexanes, 1:1); (18 mg, 64%): ^{1}H NMR ($CDCl_3$, 500 MHz): δ=4.47 (bs, 2H), 6.64 (d, J=8.4 Hz, 1H), 6.69 (dd, J=7.6, 7.4 Hz, 1H), 7.26–7.33 (m, 2H), 7.41 (d, J=7.6 Hz, 1H), 7.49 (dd, J=8.0, 7.9 Hz, 1H), 7.55 (d, J=7.9 Hz, 1H), 7.72 (d, J=7.8 Hz, 1H), 7.75 (d, J=8.0 Hz, 1H), 7.91 (s, 1H), 8.03 (bs, 1H), 8.08 (s, 1H), 8.51 (d, J=3.8 Hz, 1H), 8.62 (s, 1H); ^{13}C NMR ($CDCl_3$, 62.5 MHz): δ=44.8, 112.5, 115.2, 116.0, 117.5 (q), 121.2 (q), 123.7, 123.9, 127.6, 129.7, 133.9, 134.8, 135.3, 138.6, 146.0, 148.5, 148.7, 149.7, 168.3; HRMS (ESI) *m/z* calcd for $C_{20}H_{16}F_3N_3ONa$ [*M*+Na]$^+$: 394.1138, found: 394.1136.

2-(3,3-Diphenylallylamino)-*N*-[3-(trifluoromethyl)phenyl]benzamide (4f). Yellow solid; R_f=0.65 (EtOAc/hexanes, 1:2); (10 mg, 28%): ^{1}H NMR ($CDCl_3$, 500 MHz): δ=3.91 (d, J=6.7 Hz, 2H), 6.20 (dd, J=6.8, 6.7 Hz, 1H), 6.75 (m, 2H), 7.16–7.25 (m, 7H), 7.29–7.43 (m, 6H), 7.49 (dd, J=7.9, 7.8 Hz, 1H), 7.60 (d, J=7.4 Hz, 1H), 7.80 (d, J=7.9 Hz, 1H), 7.91 (s, 1H), 8.08 (bs, 1H); ^{13}C NMR ($CDCl_3$, 62.5 MHz): δ=42.9, 112.3, 115.2, 117.4 (q), 121.1 (q), 123.8, 126.4, 127.6, 127.7, 128.3, 128.5, 128.8, 129.7, 133.9, 138.5, 138.9, 141.9, 144.3, 149.7, 168.2; HRMS (ESI) *m/z* calcd for $C_{29}H_{23}F_3N_2ONa$ [*M*+Na]$^+$: 495.1655, found: 495.1656.

2-(Benzo[*b*]thiophen-3-ylmethylamino)-*N*-[3-(trifluoromethyl)-phenyl]benzamide (4g). White solid; R_f=0.85 (EtOAc/hexanes, 1:2); (17 mg, 53%): ^{1}H NMR ($CDCl_3$, 500 MHz): δ=4.64 (bs, 2H), 6.69 (dd, J=7.4, 7.4 Hz, 1H), 6.79 (d, J=8.4 Hz, 1H), 7.31–7.42 (m, 5H), 7.46 (dd, J=7.8, 8.0 Hz, 1H), 7.54 (d, J=7.6 Hz, 1H), 7.74 (d, J=7.9 Hz, 1H), 7.81 (d, J=7.8 Hz, 1H), 7.86 (s, 1H), 7.87 (d, J=7.4 Hz, 1H), 7.98 (s, 1H), 8.02 (bm, 1H); ^{13}C NMR ($CDCl_3$, 62.5 MHz): δ=42.0, 112.8, 115.0, 115.7, 117.3 (q), 121.1 (q), 121.6, 123.1, 123.4, 123.7, 124.3, 124.7, 127.5, 129.7, 133.2, 133.9, 137.9, 138.5, 141.1, 150.0, 168.2; HRMS (ESI) *m/z* calcd for $C_{23}H_{17}F_3N_2OSNa$ [*M*+Na]$^+$: 449.0906, found: 449.0904.

2-(4-Hydroxybenzyl)amino-*N*-[3-(trifluoromethyl)phenyl]benzamide (4h). Yellow solid; R_f=0.55 (EtOAc/hexanes, 1:2); (20 mg, 69%): ^{1}H NMR ($CDCl_3$, 500 MHz): δ=4.33 (bs, 2H), 6.66 (dd, J=7.4, 7.4 Hz, 1H), 6.71 (d, J=8.4 Hz, 1H), 6.76 (bd, J=8.4 Hz, 2H), 7.21 (bd, J=8.4 Hz, 2H), 7.31 (m, 1H), 7.39 (d, J=7.6 Hz, 1H), 7.48 (dd, J=8.0, 7.9 Hz, 1H), 7.50 (dd, J=7.8, 1.0 Hz, 1H), 7.74 (d, J=7.9, 1H), 7.86 (s, 1H), 7.91 (bs, 1H); ^{13}C NMR ($CDCl_3$, 62.5 MHz): δ=46.9, 112.8, 114.8, 115.4, 115.7, 117.4 (q), 121.1 (q), 123.7, 127.5, 128.8, 129.7, 130.9, 133.8, 138.5, 150.0, 154.9, 168.4; HRMS (ESI) *m/z* calcd for $C_{21}H_{17}F_3N_2O_2Na$ [*M*+Na]$^+$: 409.1134, found: 409.1136.

2-[(Thiazole-2-yl)methyl]amino-*N*-[3-(trifluoromethyl)phenyl]benzamide (4i). Light yellow solid; R_f=0.40 (EtOAc/hexanes, 1:2); (14 mg, 50%): ^{1}H NMR ($CDCl_3$, 500 MHz): δ=4.77 (bs, 2H), 7.71–7.76 (m, 2H), 7.26 (bm, 1H), 7.32 (dd, J=8.0, 7.6 Hz, 1H), 7.41 (d, J=7.6 Hz, 1H), 7.49 (dd, J=8.0, 7.8 Hz, 1H), 7.54 (d, J=7.8, 1H), 7.73–7.79 (m, 2H), 7.93 (s, 1H), 8.05 (bs, 1H); ^{13}C NMR ($CDCl_3$, 62.5 MHz): δ=45.6, 112.9, 116.7, 116.0, 117.4 (q), 119.4, 121.2 (q), 123.7, 127.6, 129.7, 133.8, 138.6, 142.7, 149.2, 168.1, 171.4; HRMS (ESI) *m/z* calcd for $C_{18}H_{14}F_3N_3OSNa$ [*M*+Na]$^+$: 400.0702, found: 400.0702.

2-[(Furan-2-yl)methyl]amino-*N*-[3-(trifluoromethyl)phenyl]benzamide (4j). Yellow solid; R_f=0.55 (EtOAc/hexanes, 1:2); (15 mg, 55%): ^{1}H NMR ($CDCl_3$, 500 MHz): δ=4.40 (d, J=5.1 Hz, 2H), 6.25 (m, 1H), 6.31 (m, 1H), 6.70 (m, 1H), 6.82 (d, J=8.4 Hz, 1H), 7.32–7.38 (m, 2H), 7.47 (t, J=8.0 Hz, 2H), 7.51 (dd, J=7.9, 1.4 Hz, 1H), 7.74 (d, J=7.3 Hz, 2H), 7.88 (bs, 1H), 7.95 (bs, 1H); ^{13}C NMR ($CDCl_3$, 62.5 MHz): δ=40.7, 109.7, 110.6, 112.6, 115.2, 120.4, 123.2 (q), 123.6 (q), 127.6, 129.2, 129.6, 133.8, 142.1, 143.3, 149.7, 152.3, 168.1; HRMS (ESI) *m/z* calcd for $C_{19}H_{15}F_3N_2O_2Na$ [*M*+Na]$^+$: 383.0978, found: 383.0977.

3-(*tert*-Butoxycarbonylamino)thiophene-2-carboxylic acid (6).[32] Di-*tert*-butyl dicarbonate (Boc_2O, 3.4 g, 15.6 mmol) was added dropwise to a stirred solution of methyl 3-aminothiophene-2-carboxylate **5** (800 mg, 5.1 mmol), DMAP (1.0 g, 8.2 mmol), Et_3N (2.0 mL, 14.4 mmol), and CH_2Cl_2 (8 mL) under an Ar atmosphere. After 4 h at ambient temperature, the orange solution was extracted with ice-cold HCl (1 N, 3×7 mL), ice-cold NaOH (1 N, 3×7 mL), and brine (3×7 mL). The organic extract was dried over $MgSO_4$, filtered, concentrated under reduced pressure, and the corresponding protected amine was purified by column chromatography (10% EtOAc/hexanes). The resulting yellow product was then dissolved in MeOH (60 mL) and treated with NaOH (0.6 M in H_2O/MeOH 1:20, 3.0 mL). After stirring for 6 h at ambient temperature, the solution was diluted with H_2O, and MeOH was evaporated under reduced pressure. The aqueous phase was washed with Et_2O (2×10 mL), then cooled in an ice bath and acidified to pH 2 using H_2SO_4 from a 10% *v/v* solution. The precipitate was immediately extracted with EtOAc (3×10 mL), dried over $MgSO_4$, filtered, and concentrated under reduced pressure to yield **6** (980 mg, 4 mmol, 78% over two steps): ^{1}H NMR ($CDCl_3$, 500 MHz): δ=1.54 (bs, 9H), 7.53 (d, J=5.4 Hz, 1H), 7.92 (d, J=5.4 Hz, 1H), 9.19 (s, 1H).

3-Amino-*N*-[3-(trifluoromethyl)phenyl]thiophene-2-carboxamide (8). A mixture of **6** (730 mg, 3.0 mmol) and *N*,*N*′-diisopropylcarbodiimide (DIC, 1.86 mL, 12.0 mmol) was dried by azeotropic evaporation twice with toluene. Another mixture of 3-(trifluoromethyl)aniline **1** (1.12 mL, 9.0 mmol), DMAP (1.10 g, 9.0 mmol), and DIPEA (2.10 mL, 12.3 mmol) was also dried the same way. The two mixtures were combined in dry THF (5 mL) under an Ar atmosphere and heated at 70 °C for 2 h. The reaction was then cooled to ambient temperature, diluted in EtOAc (30 mL), and extracted with saturated aqueous $NaHCO_3$ (10 mL), NH_4Cl (2×10 mL), and NaCl (2×10 mL). After drying the organic layer with $MgSO_4$, filtering, and concentrating, the coupled product was purified by column chromatography (10→15% EtOAc/hexanes) to yield compound **7**. Consequently, protected amine **7** was dissolved in CH_2Cl_2 (20 mL), and TFA (7 mL, 26%) was added in three portions over 30 min and stirred at ambient temperature. The solution was then concentrated to dryness under reduced pressure to yield amine **8** (445 mg, 52% over two steps): ^{1}H NMR ($CDCl_3$, 500 MHz): δ = 6.69 (d, J = 5.4 Hz, 1H), 7.31 (d, J = 5.4 Hz, 1H), 7.38 (bs, 1H), 7.42 (d, J = 7.9 Hz, 1H), 7.48 (dd, J = 8.0, 7.9 Hz, 1H), 7.68 (d, J = 8.0 Hz, 1H), 7.78 (s, 1H).

Compounds (9a–9j). A solution of **8** (200 mg, 0.7 mmol) and AcOH (50 μL, 2.9 mmol) in MeOH (10 mL) was divided among 10 flasks. Each solution was treated with 0.1 mmol of each aldehyde and stirred at room temperature for 12 h. In each reaction, 1.0 mL of a solution of $NaCNBH_3$ (210 mg, 3.3 mmol) in MeOH (10 mL) was added, and stirring was continued for a further 24 h at ambient temperature. The solvent was evaporated, and the residues were diluted with CH_2Cl_2 (15 mL) and extracted with saturated aqueous $NaHCO_3$ (2×10 mL) followed by saturated NaCl (2×10 mL). The organic layer was dried over $MgSO_4$, filtered, and concentrated under reduced pressure. All products were purified by column chromatography (EtOAc/hexanes).

3-(Pyridin-4-ylmethylamino)-*N*-[3-(trifluoromethyl)phenyl]thiophene-2-carboxamide (9a). Orange solid; R_f = 0.20 (EtOAc/hexanes, 1:1); (15 mg, 57%): ^{1}H NMR ($CDCl_3$, 500 MHz): δ = 4.54 (d, J = 6.4 Hz, 2H), 6.54 (d, J = 5.4 Hz, 1H), 7.23 (bs, 1H), 7.27–7.30 (m, 3H), 7.38 (d, J = 7.9 Hz, 1H), 7.47 (dd, J = 8.0, 7.9 Hz, 1H), 7.72 (d, J = 8.0 Hz, 1H), 7.91 (s, 1H), 7.99 (t, J = 5.8 Hz, 1H), 8.57 (d, J = 5.2 Hz, 2H); ^{13}C NMR ($CDCl_3$, 62.5 MHz): δ = 48.0, 101.3, 117.2 (q), 117.7, 120.8 (q), 122.1, 123.4, 129.1, 129.7, 138.6, 149.3, 149.7, 155.7, 163.6; HRMS (ESI) m/z calcd for $C_{18}H_{14}F_3N_3OSNa$ $[M+Na]^+$: 400.0702, found: 400.0702.

3-(Perfluorobenzylamino)-*N*-[3-(trifluoromethyl)phenyl]thiophene-2-carboxamide (9b). Light yellow solid; R_f = 0.70 (EtOAc/hexanes, 1:4); (29 mg, 89%): ^{1}H NMR ($CDCl_3$, 500 MHz): δ = 4.59 (d, J = 6.7 Hz, 2H), 6.86 (d, J = 5.4 Hz, 1H), 7.13 (bs, 1H), 7.32–7.37 (m, 2H), 7.44 (dd, J = 8.0, 7.9 Hz, 1H), 7.71 (d, J = 8.0 Hz, 1H), 7.81 (bs, 1H), 7.84 (m, 1H); ^{13}C NMR ($CDCl_3$, 62.5 MHz): δ = 36.9, 102.0, 117.1 (q), 117.3, 120.8 (q), 123.5, 129.1, 129.7, 138.5, 154.8, 163.3; HRMS (ESI) m/z calcd for $C_{19}H_{10}F_8N_2OSNa$ $[M+Na]^+$: 489.0278, found: 489.0280.

3-(2,5-Dihydroxybenzylamino)-*N*-[3-(trifluoromethyl)phenyl]thiophene-2-carboxamide (9c). Yellow solid; R_f = 0.40 (EtOAc/hexanes, 1:1); (18 mg, 63%): ^{1}H NMR ($CDCl_3$, 500 MHz): δ = 4.46 (bs, 2H), 6.63–6.72 (m, 3H), 6.77 (d, J = 5.4 Hz, 1H), 7.19 (s, 1H), 7.28 (d, J = 5.4 Hz, 1H), 7.37 (d, J = 7.4 Hz, 1H), 7.46 (dd, J = 8.0, 7.8 Hz, 1H), 7.68 (bs, 1H), 7.71 (d, J = 7.5 Hz, 1H), 7.82 (s, 1H); ^{13}C NMR ($CDCl_3$, 62.5 MHz): δ = 46.7, 102.0, 115.5, 117.2, 117.3 (q), 119.1, 120.9 (q), 123.6, 125.2, 128.9, 129.7, 135.4, 138.6, 148.8, 149.5, 156.0, 163.3; HRMS (ESI) m/z calcd for $C_{19}H_{15}F_3N_2O_3SNa$ $[M+Na]^+$: 431.0648, found: 431.0648.

3-(2-Hydroxy-5-nitrobenzylamino)-*N*-[3-(trifluoromethyl)phenyl]thiophene-2-carboxamide (9d). Light yellow solid; R_f = 0.35 (EtOAc/hexanes, 1:1); (26 mg, 85%): ^{1}H NMR ($CDCl_3$, 500 MHz): δ = 4.52 (bs, 2H), 6.76 (d, J = 5.4 Hz, 1H), 6.82 (d, J = 8.8 Hz, 1H), 7.30 (s, 1H), 7.32–7.37 (m, 2H), 7.43 (dd, J = 7.9, 7.8 Hz, 1H), 7.65 (d, J = 7.9 Hz, 1H), 7.76 (m, 1H), 7.83 (s, 1H), 8.02 (dd, J = 8.9, 2.5 Hz, 1H), 8.11 (m, 1H); ^{13}C NMR ($CDCl_3$, 62.5 MHz): δ = 47.4, 105.2, 116.7, 117.7 (q), 119.0, 121.3 (q), 123.9, 124.5, 124.9, 125.5, 129.4, 129.7, 138.1, 141.3, 155.3, 161.7, 163.3; HRMS (ESI) m/z calcd for $C_{19}H_{14}F_3N_3O_4SNa$ $[M+Na]^+$: 460.0549, found: 460.0546.

3-(Pyridin-3-ylmethylamino)-*N*-[3-(trifluoromethyl)phenyl]thiophene-2-carboxamide (9e). Yellow solid; R_f = 0.20 (EtOAc/hexanes, 1:1); (25 mg, 95%): ^{1}H NMR ($CDCl_3$, 500 MHz): δ = 4.52 (d, J = 6.0 Hz, 2H), 6.63 (d, J = 5.4 Hz, 1H), 7.21 (bs, 1H), 7.24–7.29 (m, 2H), 7.36 (d, J = 7.6 Hz, 1H), 7.45 (dd, J = 8.0, 7.8 Hz, 1H), 7.69 (dd, J = 8.9, 8.8 Hz, 2H), 7.87 (s, 1H), 7.90 (m, 1H), 8.53 (m, 1H), 8.60 (s, 1H); ^{13}C NMR ($CDCl_3$, 62.5 MHz): δ = 46.7, 101.2, 117.1 (q), 117.8, 120.7 (q), 123.4, 123.9, 125.2, 129.1, 129.6, 135.0, 138.7, 148.8, 148.9, 155.8, 163.6; HRMS (ESI) m/z calcd for $C_{18}H_{14}F_3N_2OSNa$ $[M+Na]^+$: 400.0702, found: 400.0701.

3-(3,3-Diphenylallylamino)-*N*-[3-(trifluoromethyl)phenyl]thiophene-2-carboxamide (9f). Bright yellow solid; R_f = 0.75 (EtOAc/hexanes, 1:2); (30 mg, 89%): ^{1}H NMR ($CDCl_3$, 500 MHz): δ = 3.89 (t, J = 6.1 Hz, 2H), 6.07 (t, J = 6.6 Hz, 1H), 6.46 (d, J = 5.5 Hz, 1H), 7.04 (s, 1H), 7.10–7.21 (m, 8H), 7.24–7.38 (m, 5H), 7.49 (m, 1H), 7.62 (d, J = 7.8 Hz, 1H), 7.78 (s, 1H); ^{13}C NMR ($CDCl_3$, 62.5 MHz): δ = 44.6, 100.4, 117.0 (q), 118.1, 120.5 (q), 123.3, 125.9, 127.6, 127.7, 127.8, 128.3, 128.5, 128.8, 129.6, 129.9, 138.8, 139.2, 141.7, 144.5, 155.9, 163.5; HRMS (ESI) m/z calcd for $C_{27}H_{21}F_3N_2OSNa$ $[M+Na]^+$: 501.1219, found: 501.1217.

3-(Benzo[*b*]thiophen-3-ylmethylamino)-*N*-[3-(trifluoromethyl)phenyl]thiophene-2-carboxamide (9g). Yellow solid; R_f = 0.60 (EtOAc/hexanes, 1:3); (21 mg, 69%): ^{1}H NMR ($CDCl_3$, 500 MHz): δ = 4.72 (d, J = 5.3 Hz, 2H), 6.73 (d, J = 5.4 Hz, 1H), 7.19 (s, 1H), 7.27 (d, J = 5.4 Hz, 1H), 7.31–7.45 (m, 5H), 7.70 (d, J = 7.0 Hz, 1H), 7.79 (d, J = 7.7 Hz, 1H), 7.83–7.90 (m, 3H); ^{13}C NMR ($CDCl_3$, 62.5 MHz): δ = 44.0, 117.1 (q), 118.1, 120.6 (q), 121.5, 123.2, 123.4, 123.5, 124.4, 124.8, 128.9, 129.6, 133.5, 137.7, 138.7, 141.1, 156.1, 163.6; HRMS (ESI) m/z calcd for $C_{21}H_{15}F_3N_2OS_2Na$ $[M+Na]^+$: 455.0470, found: 455.0472.

3-(4-Hydroxybenzylamino)-*N*-[3-(trifluoromethyl)phenyl]thiophene-2-carboxamide (9h). Light yellow solid; R_f = 0.30 (EtOAc/hexanes, 1:1); (25 mg, 91%): ^{1}H NMR ($CDCl_3$, 500 MHz): δ = 4.40 (d, J = 5.0 Hz, 2H), 6.68 (d, J = 5.4 Hz, 1H), 6.76 (d, J = 8.3 Hz, 2H), 7.15–7.19 (m, 3H), 7.25 (d, J = 5.4 Hz, 1H), 7.34 (d, J = 7.7 Hz, 1H), 7.43 (dd, J = 7.9, 7.7 Hz, 1H), 7.67–7.74 (m, 2H), 7.83 (s, 1H); ^{13}C NMR ($CDCl_3$, 62.5 MHz): δ = 48.7, 100.3, 115.7, 117.2 (q), 118.2, 120.6 (q), 123.5 128.7, 129.0, 129.6, 130.9, 138.7, 155.2, 156.3, 163.7; HRMS (ESI) m/z calcd for $C_{19}H_{15}F_3N_2O_2SNa$ $[M+Na]^+$: 415.0698, found: 415.0700.

3-(Thiazol-2-ylmethylamino)-*N*-[3-(trifluoromethyl)phenyl]thiophene-2-carboxamide (9i). Light yellow solid; R_f = 0.20 (EtOAc/hexanes, 1:2); (20 mg, 75%): ^{1}H NMR ($CDCl_3$, 500 MHz): δ = 4.81 (d, J = 6.3 Hz, 2H), 6.72 (d, J = 5.4 Hz, 1H), 7.22 (s, 1H), 7.25–7.29 (m, 2H), 7.36 (d, J = 7.6 Hz, 1H), 7.46 (dd, J = 7.8, 7.6 Hz, 1H), 7.72 (d, J = 7.8 Hz, 1H), 7.75 (d, J = 3.2 Hz, 1H), 7.89 (s, 1H), 8.09 (m, 1H); ^{13}C NMR ($CDCl_3$, 62.5 MHz): δ = 47.4, 102.3, 117.2 (q), 118.2, 119.6, 120.8 (q), 123.4, 128.8, 129.6, 138.7, 142.9, 155.4, 163.4, 170.9;

HRMS (ESI) *m/z* calcd for $C_{16}H_{12}F_3N_3OS_2Na$ $[M+Na]^+$: 406.0266, found: 406.0267.

3-(Furan-2-ylmethylamino)-*N*-[3-(trifluoromethyl)phenyl]thiophene-2-carboxamide (9j). Yellow solid; $R_f = 0.35$ (EtOAc/hexanes, 1:4); (16 mg, 62%): ^{1}H NMR ($CDCl_3$, 500 MHz): $\delta = 4.45$ (bs, 2H), 6.22 (m, 1H), 6.31 (m, 1H), 6.80 (d, $J = 5.4$ Hz, 1H), 7.17 (s, 1H), 7.29 (d, $J = 5.4$ Hz, 1H), 7.33–7.37 (m, 2H), 7.44 (dd, $J = 8.0$, 7.9, 1H), 7.70 (d, $J = 7.9$ Hz, 2H), 7.86 (s, 1H); ^{13}C NMR ($CDCl_3$, 62.5 MHz): $\delta = 42.5$, 101.2, 107.2, 110.5, 117.0 (q), 118.1, 120.6 (q), 123.3, 128.8, 129.6, 138.8, 142.3, 152.5, 155.8, 163.5; HRMS (ESI) *m/z* calcd for $C_{17}H_{13}F_3N_2O_2S$ Na $[M+Na]^+$: 389.0542, found: 389.0540.

Computational methods

Because the X-ray crystal structure coordinates of AAL993 in complex with the catalytic domain of VEGFR-2 are not yet available at the PDB,[27] the highest-resolution (1.71 Å) structure, with the fewest missing residues, of a 4-aminofuro[2,3-*d*]pyrimidine compound with VEGFR-2 (PDB entry 1YWN) was used.[18] The previously determined crystal structure of the VEGFR-2 kinase domain free of ligand (PDB entry 1VR2)[16] was discarded owing to: a) lower resolution (2.40 Å), b) more missing residues in the activation loop, and c) a greater number of disordered side chain atoms. However, superimposition of 1VR2 with 1YWN displays minor differences between the two structures (backbone RMSD = 0.50 Å). The residue numbering used herein is according to 1VR2, which differs from 1YWN by +2. Water molecules and ligands were deleted from the PDB file. Given that the constructs used for crystallization lack the central 50 residues (residues 942–991) of the 68-residue kinase insert domain, residues Phe 935, Val 936, and Pro 937 were removed to facilitate linking of Glu 934 and Phe 999 (Cα–Cα distance of 4.8 Å). The missing residues Phe 1047–Asp 1052 (where Phe 1047 and Gly 1048 belong to the DFG motif) were modeled using the corresponding coordinates from PDB entry 2OH4,[21] with VEGFR-2 adopting the DFG-out conformation as previously reported for AAL993.[27] For the missing residues Lys 871–Ala 874, Cα atoms were added manually, and the rest of the missing atoms were automatically completed by the XLEaP module of AMBER 9.[33] Histidine protonation states were predicted at pH 7.0 using the program H++ with standard parameters for the Poisson–Boltzmann electrostatics calculation method.[34] After visual inspection for H-bonding ability of each histidine with neighboring residues, all nine histidines were set to be protonated at $N^{\varepsilon 2}$ only. The other basic and acidic residues were assigned their standard protonation states. The parm99 AMBER force field was employed for the protein atoms,[35] and the TIP3P water model was used for the solvent.[36] The phosphorylation site residues Tyr 1054 and Tyr 1059 were assigned AMBER force field parameters as reported previously.[37] VEGFR-2 ligands taken from crystal structures were assigned AM1-BCC charges[38] and GAFF parameters[39] using the ANTECHAMBER module of AMBER 9. Coordinates for the designed scaffolds were produced from SMILES representation using OMEGA 2.2,[40] and were then assigned AM1-BCC charges using the MOLCHARGE 1.3 module of QUACPAC.[41] The electrostatic potential of geometry-optimized ligands was calculated at the Hartree–Fock level with 6-31G* basis using Gaussian 98.

To relax the protein from crystal packing contacts and to optimize the position of the modeled atoms, energy minimization was performed in implicit solvent using a generalized Born solvation model (GB^{HCT})[42] with a cutoff of 16 Å for the nonbonded interactions. An initial 2000-step round of minimization was carried out using the steepest-descent method with positional restraints of 50 kcal mol^{-1} Å^{-2} force constant to the Cα atoms that were determined in the crystal structure. Subsequently, a second round of 1000 steps of unrestrained energy minimization with conjugate gradients was performed, which resulted in a model with heavy-atom RMSD = 0.49 Å with respect to the crystal structure. This structure was used for docking calculations and subsequent MD simulations. A model of VEGFR-2 kinase domain with both Tyr 1054 and Tyr 1059 phosphorylated was prepared in the same way. The program AutoDock 3[43] was used for docking of the inhibitors to the model of the VEGFR-2 kinase domain, and AutoDockTools 1.5 was used for examination of the docking results. Protein and ligands were treated with the united-atom approximation by merging all nonpolar hydrogen atoms. Kollman partial charges were assigned to protein atoms, AM1-BCC charges to ligands, while charges and van der Waals parameters for the two phosphate groups were taken from the AMBER database. The interaction grid maps were centered at the ATP binding site and comprised 81×81×81 points of 0.25 Å spacing. The Lamarckian genetic algorithm was used with the following parameters: a population size of 50 individuals, a maximum number of 1.5×10^6 energy evaluations and a maximum number of 27 000 generations, an elitism value of 1.0, a mutation rate of 0.02, and a crossover rate of 0.80. For most of the calculations, 100 docking rounds were performed with step sizes of 0.25 Å for translations and 5° for orientations and torsions. Docked conformations were clustered within 1.5 Å RMS positional deviation tolerance.

Molecular dynamics (MD) calculations were carried out using the SANDER and PMEMD programs of AMBER 9.[33] Periodic boundary conditions were imposed by the particle mesh Ewald method, with a limit of 8 Å for the direct space sum. Numerical integration was performed with a 2-fs time step, and all bonds involving hydrogen atoms were constrained with SHAKE. Temperature and pressure controls were imposed using a Berendsen-type algorithm[44] with coupling constants of 1.0 and 2.0 ps, respectively. Either the free protein or the protein–ligand complexes were immersed in isometric truncated octahedron water boxes, and then an appropriate number of counterions were added to neutralize the system charge. The following procedure was carried out to optimize the water positions and to equilibrate the temperature and pressure of the systems: a) energy minimization for 1000 steps using the steepest-descent method with harmonic restraints of 50 kcal mol^{-1} Å^{-2} force constant on all solute atoms; b) restrained constant volume dynamics (NVT ensemble) at 300 K for 30 ps; c) a second energy minimization for 1000 steps with 10 kcal mol^{-1} Å^{-2} restraints on all protein Cα atoms; d) the temperature was then gradually increased to 300 K within six rounds of 5-ps constant volume dynamics (NVT), while solute atoms were restrained with 10 kcal mol^{-1} Å^{-2}; e) restraints were then gradually released within 20 ps in the NVT ensemble at 300 K; f) the density of the systems was increased from ~0.88 to ~1.04 g cm^{-3} during 150 ps of constant pressure dynamics (NPT ensemble). Subsequently, production runs were carried out under physiological conditions (300 K, 1 atm) in the NPT ensemble for a total time of 10 ns. The translational center-of-mass motion was removed every 1000 steps, and trajectories were updated every 500 steps. Analysis and visual inspection of the MD trajectories were performed using the PTRAJ module of AMBER 9 and VMD 1.8.6.[45] Figures were also prepared with VMD, while plots were generated using the program GRACE. All calculations were carried out on an Intel Quad Core workstation, running an X86_64 Linux 2.6-smp kernel, while AMBER 9 was compiled using the Intel Fortran 9.1 compilers.

Biology and screening assays

Cell culture. HeLa (human cervical epithelioid carcinoma) cells were cultured in Dulbecco's modified Eagle's medium (DMEM) supplemented with 2 mM L-glutamine (PAA) and 10% fetal calf serum (PAA). HUVECp (human umbilical vein endothelial cells pooled from multiple isolates; Cascade Biologics) were cultured in Medium 200 supplemented with LSGS (Cascade Biologics). Cells used in experiments were between passages 3 and 5. All cells were maintained at 37 °C under 5% CO_2 as exponentially growing monolayers.

Cell proliferation assays. The ability of the compounds to inhibit proliferation of cell growth was determined using the MTT assay, as described previously.[30] Briefly, 4×10^5 cells were trypsinized and seeded into 96-well microplates (Orange Scientific, Belgium) in complete medium up to a volume of 100 μL. Cells were incubated for 24 h at 37 °C in an atmosphere containing 5% CO_2. Medium was removed, and fresh medium was added to each well, containing the appropriate concentration of each compound in a total volume of 100 μL, and cells were incubated for an additional 24 h. Afterward the supernatant was removed, and cells were washed twice with 200 μL 1×PBS. 1-(4,5-Dimethylthiazol-2-yl)-3,5-diphenylformazan (MTT; Sigma Chemical Co., St. Louis, MO, USA) diluted in complete medium to a final concentration of 1 mg mL^{-1}, was added to each well in a volume of 100 μL. The plate was incubated for 1.5 h at 37 °C, so that MTT (yellow) can be transformed into formazan crystals (purple) by the viable cells. The supernatant was removed, and the formazan crystals were solubilized for 10 min upon addition of 100 μL DMSO. The absorbance of each cell lysate solution was measured at 550 nm. Results from the MTT assays are expressed as the mean value of the absorption at 550 nm ± standard deviation from two independent experiments, which were repeated three times each. IC_{50} values represent the concentration of each compound required for 50% decrease in cell viability, and were estimated using sigmoid fitting.

In vitro kinase assays. IC_{50} values for the inhibition of VEGFR-2 (KDR) kinase using individual compounds were measured with an HTScan® VEGFR-2 kinase assay kit (Cell Signaling Technology, USA), following the colorimetric ELISA protocol provided by the manufacturer. Recombinant human GST–VEGFR-2 kinase (Val 789–Val 1356), biotinylated peptide substrate, and phosphotyrosine antibody for the detection of phosphorylated substrate were all supplied within the kit. Before the reaction, a 2× ATP/substrate cocktail ([ATP] = 40 μM, [substrate] = 3 μM) and a 4× reaction cocktail ([enzyme] = 8 ng μL^{-1} in DTT/kinase buffer) were prepared. All compounds were dissolved in DMSO and diluted with deionized H_2O to a final DMSO concentration of 4% (*v*/*v*). Control experiments were carried out by adding DMSO alone; that is, no test compounds were added into reactions containing either 2× ATP/substrate and 4× reaction cocktail (A_{max} control), or 2× ATP/substrate only (A_{min} control); 4× reaction cocktail (12.5 μL) was incubated at room temperature for 5 min with 12.5 μL of the pre-diluted compound of interest (concentrations per well ranging from 1 to 500 nM) as well as with 12.5 μL of A_{max} and A_{min} control samples; 2× ATP/substrate cocktail (25 μL) was added to pre-incubated cocktail/compound (25 μL per well) in a 96-well reaction plate. The final assay conditions per well for a 50-μL reaction were the following: 60 mM HEPES (pH 7.5), 5 mM $MgCl_2$, 5 mM $MnCl_2$, 3 μM Na_3VO_4, 1.25 mM DTT, 20 μM ATP, 1.5 μM peptide, and 100 ng VEGFR-2 kinase. The reaction plate was incubated at room temperature for 30 min. Each reaction was terminated by the addition of 'stop' buffer (50 μL per well; 50 mM EDTA, pH 8). Subsequently, 25 μL of each reaction and 75 μL deionized H_2O per well were transferred to a Delfia® 96-well streptavidin-coated yellow plate (PerkinElmer Life Sciences). After 1 h at room temperature, the solution was removed, and the plate was washed with PBS/T (1×PBS with 0.05% Tween-20; 3×200 μL per well). The wells were then incubated with primary antibody (100 μL per well), phosphotyrosine mAb (P-Tyr-100), 1:1000 in PBS/T with 1% BSA, for 1 h at room temperature. The solutions were then removed, and the wells were washed with PBS/T (3×200 μL per well). The wells were then incubated at room temperature for 30 min with anti-mouse IgG HRP-labeled secondary antibody (100 μL per well), 1:500 in PBS/T with 1% BSA (Cell Signaling Technology, USA). Unbound antibody was removed, and the plate was washed with PBS/T (5×200 μL per well). TMB substrate (100 μL; Cell Signaling Technology, USA) was added to each well, and the plate was incubated at room temperature for 5 min. Stop solution (100 μL; Cell Signaling Technology, USA) was added to each well, and after incubating at room temperature for 5 min, the absorbance at 450 nm was recorded with an ELISA plate reader. Percent inhibition values were calculated according to Equation (1):

$$\%\ \text{Inhibition} = \{1-[(A_{\text{measured}}-A_{\text{min}})/(A_{\text{max}}-A_{\text{min}})]\}\times 100 \qquad (1)$$

for which $A_{measured}$ is the mean value from two independent experiments. Each IC_{50} value was determined by plotting the percent inhibition as a function of log([compound] in nM) using a sigmoidal fit, and are presented in Table 1.

In vitro HUVEC tube formation assays. The in vitro angiogenesis assay kit, using ECMatrix™ gel (Chemicon®), was used according to the manufacturer's protocol. Briefly, matrix solution was solidified on 96-well plates. HUVEC (up to passage 4) cell suspension of 1×10^5 cells mL^{-1} was prepared in medium containing potential angiogenesis inhibitors at concentrations of 10 and 50 μM, in the presence or absence of VEGF at 50 ng mL^{-1}. All compounds were diluted in 4% DMSO, (final concentration of DMSO in culture was 1%). Cells were cultured in duplicates at a concentration of 1×10^4 cells per well in ECMatrix™-coated plates. Tube formation and cellular networks were monitored under a light microscope. Cells were stained with calcein, and images were acquired with a digital camera under a fluorescence microscope.

Acknowledgements

This work was supported by the research project ENTER2004 (04EP63), which is co-financed by the E.U.–European Social Fund (75%) and the Greek Ministry of Development–GSRT (25%).

Keywords: angiogenesis · drug design · inhibitors · medicinal chemistry · molecular dynamics · VEGFR-2

[1] D. J. Hicklin, L. M. Ellis, *J. Clin. Oncol.* **2004**, *23*, 1011 – 1027.
[2] N. Ferrara, R. S. Kerbel, *Nature* **2005**, *438*, 967 – 974.
[3] G. Neufeld, T. Cohen, S. Gengrinovitch, Z. Poltorak, *FASEB J.* **1999**, *13*, 9 – 22.
[4] N. Ferrara, *Nat. Rev. Cancer* **2002**, *2*, 795 – 803.
[5] N. Ferrara, *Endocr. Rev.* **2004**, *25*, 581 – 611.
[6] N. Ferrara, K. J. Hillan, H. P. Gerber, W. Novotny, *Nat. Rev. Drug Discovery* **2004**, *3*, 391 – 400.
[7] M. Shibuya, *Int. J. Biochem. Cell Biol.* **2001**, *33*, 409 – 420.
[8] N. Ferrara, H. P. Gerber, J. LeCouter, *Nat. Med.* **2003**, *9*, 669 – 676.
[9] T. Tammela, B. Enholm, K. Alitalo, K. Paavonen, *Cardiovasc. Res.* **2005**, *65*, 550 – 563.
[10] T. Takahashi, S. Yamaguchi, K. Chida, M. Shibuya, *EMBO J.* **2001**, *20*, 2768 – 2778.

[11] T. L. Underiner, B. Ruggeri, D. E. Gingrich, *Curr. Med. Chem.* **2004**, *11*, 731 – 745.
[12] G. Kesisis, H. Broxterman, G. Giaccone, *Curr. Pharm. Des.* **2007**, *13*, 2795 – 2809.
[13] H. Zhong, J. P. Bowen, *Curr. Top. Med. Chem.* **2007**, *7*, 1379 – 1393.
[14] A. Kiselyov, K. V. Balakin, S. E. Tkachenko, *Expert Opin. Invest. Drugs* **2007**, *16*, 83 – 107.
[15] S. Schenone, F. Bondavalli, M. Botta, *Curr. Med. Chem.* **2007**, *14*, 2495 – 2516.
[16] M. A. McTigue, J. A. Wickersham, C. Pinko, R. E. Showalter, C. Parast V, A. Tempczyk-Russell, M. R. Gehring, B. Mroczkowski, K. Chen-Chen, J. E. Villafranca, K. Appelt, *Structure* **1999**, *7*, 319 – 330.
[17] P. A. Harris, M. Cheung, R. N. Hunter Iii, M. L. Brown, J. M. Veal, R. T. Nolte, L. Wang, W. Liu, R. M. Crosby, J. H. Johnson, A. H. Epperly, R. Kumar, D. K. Luttrell, J. A. Stafford, *J. Med. Chem.* **2005**, *48*, 1610 – 1619.
[18] Y. Miyazaki, S. Matsunaga, J. Tang, Y. Maeda, M. Nakano, R. J. Philippe, M. Shibahara, W. Liu, H. Sato, L. Wang, R. T. Nolte, *Bioorg. Med. Chem. Lett.* **2005**, *15*, 2203 – 2207.
[19] B. L. Hodous, S. D. Geuns-Meyer, P. E. Hughes, B. K. Albrecht, S. Bellon, J. Bready, S. Caenepeel, V. J. Cee, S. C. Chaffee, A. Coxon, M. Emery, J. Fretland, P. Gallant, Y. Gu, D. Hoffman, R. E. Johnson, R. Kendall, J. L. Kim, A. M. Long, M. Morrison, P. R. Olivieri, V. F. Patel, A. Polverino, P. Rose, P. Tempest, L. Wang, D. A. Whittington, H. Zhao, *J. Med. Chem.* **2007**, *50*, 611 – 626.
[20] M. H. Potashman, J. Bready, A. Coxon, T. M. Demelfi, Jr., L. DiPietro, N. Doerr, D. Elbaum, J. Estrada, P. Gallant, J. Germain, Y. Gu, J. C. Harmange, S. A. Kaufman, R. Kendall, J. L. Kim, G. N. Kumar, A. M. Long, S. Neervannan, V. F. Patel, A. Polverino, P. Rose, S. Van Der Plas, D. Whittington, R. Zanon, H. Zhao, *J. Med. Chem.* **2007**, *50*, 4351 – 4373.
[21] M. Hasegawa, N. Nishigaki, Y. Washio, K. Kano, P. A. Harris, H. Sato, I. Mori, R. I. West, M. Shibahara, H. Toyoda, L. Wang, R. T. Nolte, J. M. Veal, M. Cheung, *J. Med. Chem.* **2007**, *50*, 4453 – 4470.
[22] J. C. Harmange, M. M. Weiss, J. Germain, A. J. Polverino, G. Borg, J. Bready, D. Chen, D. Choquette, A. Coxon, T. DeMelfi, L. DiPietro, N. Doerr, J. Estrada, J. Flynn, R. F. Graceffa, S. P. Harriman, S. Kaufman, D. S. La, A. Long, M. W. Martin, S. Neervannan, V. F. Patel, M. Potashman, K. Regal, P. M. Roveto, M. L. Schrag, C. Starnes, A. Tasker, Y. Teffera, L. Wang, R. D. White, D. A. Whittington, R. Zanon, *J. Med. Chem.* **2008**, *51*, 1649 – 1667.
[23] D. S. La, J. Belzile, J. V. Bready, A. Coxon, T. DeMelfi, N. Doerr, J. Estrada, J. C. Flynn, S. R. Flynn, R. F. Graceffa, S. P. Harriman, J. F. Larrow, A. M. Long, M. W. Martin, M. J. Morrison, V. F. Patel, P. M. Roveto, L. Wang, M. M. Weiss, D. A. Whittington, Y. Teffera, Z. Zhao, A. J. Polverino, J. C. Harmange, *J. Med. Chem.* **2008**, *51*, 1695 – 1705.
[24] E. Hu, A. Tasker, R. D. White, R. K. Kunz, J. Human, N. Chen, R. Bürli, R. Hungate, P. Novak, A. Itano, X. Zhang, V. Yu, Y. Nguyen, Y. Tudor, M. Plant, S. Flynn, Y. Xu, K. L. Meagher, D. A. Whittington, G. Y. Ng, *J. Med. Chem.* **2008**, *51*, 3065 – 3068.
[25] G. Bold, K. H. Altmann, J. Frei, M. Lang, P. W. Manley, P. Traxler, B. Wietfeld, J. Brüggen, E. Buchdunger, R. Cozens, S. Ferrari, P. Furet, F. Hofmann, G. Martiny-Baron, J. Mestan, J. Rösel, M. Sills, D. Stover, F. Acemoglu, E. Boss, R. Emmenegger, L. Lässer, E. Masso, R. Roth, C. Schlachter, W. Vetterli, D. Wyss, J. M. Wood, *J. Med. Chem.* **2000**, *43*, 2310 – 2323.
[26] P. W. Manley, P. Furet, G. Bold, J. Brüggen, J. Mestan, T. Meyer, C. R. Schnell, J. Wood, M. Haberey, A. Huth, M. Krüger, A. Menrad, E. Ottow, D. Seidelmann, G. Siemeister, K. H. Thierauch, *J. Med. Chem.* **2002**, *45*, 5687 – 5693.
[27] P. W. Manley, G. Bold, J. Brüggen, G. Fendrich, P. Furet, J. Mestan, C. Schnell, B. Stolz, T. Meyer, B. Meyhack, W. Stark, A. Strauss, J. Wood, *Biochim. Biophys. Acta Proteins Proteomics* **2004**, *1697*, 17 – 27.
[28] M. Huse, J. Kuriyan, *Cell* **2002**, *109*, 275 – 282.
[29] P. Cozzini, G. E. Kellogg, F. Spyrakis, D. J. Abraham, G. Costantino, A. Emerson, F. Fanelli, H. Gohlke, L. A. Kuhn, G. M. Morris, M. Orozco, T. A. Pertinhez, M. Rizzi, C. A. Sotriffer, *J. Med. Chem.* **2008**, *51*, 6237 – 6255.
[30] T. Mosmann, *J. Immunol. Methods* **1983**, *65*, 55 – 63.
[31] L. N. Johnson, M. E. M. Noble, D. J. Owen, *Cell* **1996**, *85*, 149 – 158.
[32] S. Foister, M. A. Marques, R. M. Doss, P. B. Dervan, *Bioorg. Med. Chem.* **2003**, *11*, 4333 – 4340.
[33] D. A. Case, T. E. Cheatham Iii, T. Darden, H. Gohlke, R. Luo, K. M. Merz, Jr., A. Onufriev, C. Simmerling, B. Wang, R. J. Woods, *J. Comput. Chem.* **2005**, *26*, 1668 – 1688.
[34] J. C. Gordon, J. B. Myers, T. Folta, V. Shoja, L. S. Heath, A. Onufriev, *Nucleic Acids Res.* **2005**, *33*, W368 – W371.
[35] W. D. Cornell, P. Cieplak, C. I. Bayly, I. R. Gould, K. M. Merz, Jr., D. M. Ferguson, D. C. Spellmeyer, T. Fox, J. W. Caldwell, P. A. Kollman, *J. Am. Chem. Soc.* **1995**, *117*, 5179 – 5197.
[36] W. L. Jorgensen, J. Chandrasekhar, J. D. Madura, R. W. Impey, M. L. Klein, *J. Chem. Phys.* **1983**, *79*, 926 – 935.
[37] N. Homeyer, A. H. C. Horn, H. Lanig, H. Sticht, *J. Mol. Model.* **2006**, *12*, 281 – 289.
[38] A. Jakalian, D. B. Jack, C. I. Bayly, *J. Comput. Chem.* **2002**, *23*, 1623 – 1641.
[39] J. Wang, R. M. Wolf, J. W. Caldwell, P. A. Kollman, D. A. Case, *J. Comput. Chem.* **2004**, *25*, 1157 – 1174.
[40] R. Kristam, V. J. Gillet, R. A. Lewis, D. Thorner, *J. Chem. Inf. Model.* **2005**, *45*, 461 – 476.
[41] OpenEye Scientific Software, http://eyesopen.com (accessed October 28, 2009).
[42] V. Tsui, D. A. Case, *Biopolymers* **2000**, *56*, 275 – 291.
[43] G. M. Morris, D. S. Goodsell, R. S. Halliday, R. Huey, W. E. Hart, R. K. Belew, A. J. Olson, *J. Comput. Chem.* **1998**, *19*, 1639 – 1662.
[44] H. J. C. Berendsen, J. P. M. Postma, W. F. Van Gunsteren, A. Dinola, J. R. Haak, *J. Chem. Phys.* **1984**, *81*, 3684 – 3690.
[45] W. Humphrey, A. Dalke, K. Schulten, *J. Mol. Graph.* **1996**, *14*, 33 – 38.

Received: September 4, 2009
Revised: October 22, 2009
Published online on November 17, 2009

